



Internal electric field engineering step-scheme-based heterojunction using lead-free $\text{Cs}_3\text{Bi}_2\text{Br}_9$ perovskite-modified In_4SnS_8 for selective photocatalytic CO_2 reduction to CO

Zhenzong Zhang^{a,b}, Meiyang Wang^{a,b}, Zexu Chi^{a,b}, Wenjie Li^c, Han Yu^{a,d,*}, Nan Yang^a, Hongbing Yu^{a,b,*}

^a College of Environmental Science and Engineering, Nankai University, Tianjin 300350, PR China

^b Guangdong-Hong Kong-Macao Greater Bay Area Environmental Technology Research Center, Shenzhen Research Institute of Nankai University, Shenzhen 518063, PR China

^c School of Ecology and Environment, Zhengzhou University, Zhengzhou 450001, PR China

^d Department of Water Resources Engineering, Lund University, Lund 22100, Sweden

ARTICLE INFO

Keywords:

CO_2 reduction
Photocatalysis
Internal electric field
 $\text{Cs}_3\text{Bi}_2\text{Br}_9$ perovskite
 In_4SnS_8

ABSTRACT

This study focuses on improving photocatalytic CO_2 reduction reaction (CRR) activity and modulating product selectivity. An $\text{In}_4\text{SnS}_8/\text{Cs}_3\text{Bi}_2\text{Br}_9$ -X (ISS/CBB-X) heterojunction is prepared using novel lead-free $\text{Cs}_3\text{Bi}_2\text{Br}_9$ perovskite quantum dot-modified In_4SnS_8 , which shows considerable potential as photocatalysts for CRRs under visible light. The optimised ISS/CBB photocatalyst exhibits high activity and CO selectivity with a CO yield and selectivity of $9.55 \mu\text{mol g}^{-1} \text{h}^{-1}$ and 92.9%, respectively, 3.8 and 1.5 times higher than those of pristine ISS, respectively. Moreover, the step-scheme (S-scheme) mechanism can be fully confirmed via in situ irradiated X-ray photoelectron spectroscopy, in situ electron spin resonance, femtosecond time-resolved absorption spectroscopy and density functional theory calculations. Based on in situ diffuse reflectance spectra and theoretical investigations, the ISS/CBB shows a decreased energy barrier towards CO_2 reduction to CO through an adsorbed $^*\text{COOH}$ intermediate. This study contributes to the further understanding of fabricating efficient S-scheme-based photocatalysts for selective CRR.

1. Introduction

With the continuous progression of society, energy demand is increasing and CO_2 emission levels are rising exponentially [1]. Thus, issues concerning the energy crisis and environmental pollution must be addressed promptly [2]. Researchers have developed diverse CO_2 conversion pathways, including biochemical, electrochemical, thermochemical and photochemical reactions [3–5]. Notably, the use of solar energy for CO_2 conversion to a high-density hydrocarbon fuel is a promising approach. In linear CO_2 molecules, the dissociation energy of C=O bonds can reach $\sim 750 \text{ kJ/mol}$, affording the ultra-high stability of CO_2 molecules [6,7].

Currently, a series of photocatalysts for CO_2 reduction has been explored, including metal oxides, layered double hydroxides and non-metallic semiconductors [8–11]. Unfortunately, the CO_2 conversion efficiency of single photocatalysts is relatively low and cannot meet

large-scale industrial applications [10]. Increasing the visible light absorption range, photogenerated carrier transport efficiency and effective reaction sites of photocatalysts are all effective approaches for improving photocatalysts for photocatalytic CO_2 reduction.

The photocatalytic CO_2 reduction process can be divided into three steps: CO_2 adsorption activation, reduction process and product desorption. Carbon in CO_2 shows the highest oxidation state and can be reduced to various products with different numbers of electrons and protons [7,12]. For example, H_2O is a common proton donor in the CO_2 reduction process. During the reaction, H_2O can be directly reduced to H_2 via the hydrogen evolution reaction process and the competing reaction will influence the CO_2 reduction process [13]. Therefore, achieving a high-selectivity target product is the goal of a CO_2 reduction reaction (CRR). Unfortunately, owing to the low selectivity of the products, multiple products are combined, rendering the separation of individual products difficult.

* Corresponding authors at: College of Environmental Science and Engineering, Nankai University, Tianjin 300350, PR China.

E-mail addresses: yhh20212022@gmail.com (H. Yu), hongbingyu1130@sina.com (H. Yu).

<https://doi.org/10.1016/j.apcatb.2022.121426>

Received 8 December 2021; Received in revised form 21 March 2022; Accepted 17 April 2022

Available online 20 April 2022

0926-3373/© 2022 Published by Elsevier B.V.

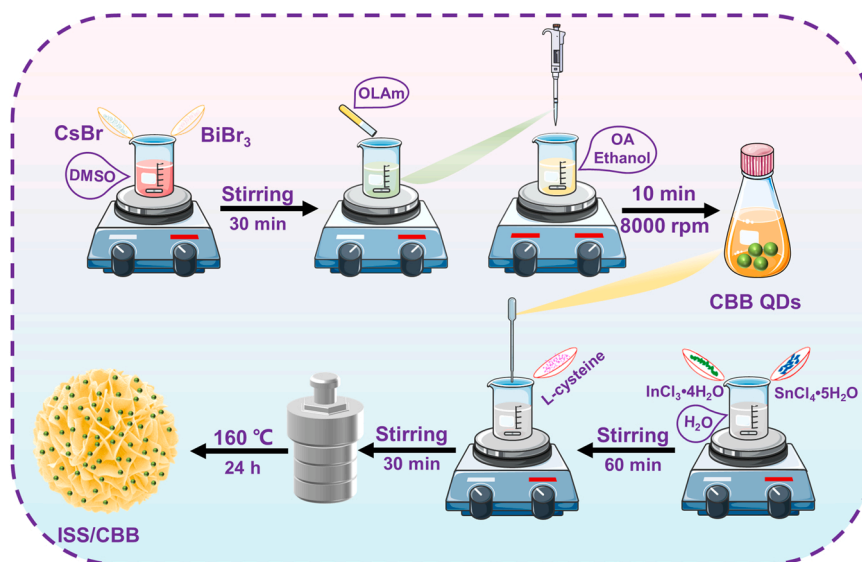


Fig. 1. Schematic illustration of the synthesis processes of CBB QDs anchored on ISS surface.

Thus, improved CO_2 adsorption and effective CO_2 desorption are critical factors for enhancing photocatalytic CO_2 conversion efficiency and product selectivity. The rational design of high-activity and -selectivity photocatalysts is particularly important. Transition metal sulphides are increasingly used in photocatalytic CO_2 reduction systems owing to their unique electronic structure and optical properties [9]. In particular, In_4SnS_8 exhibits excellent stability as well as a suitable bandgap, owing to its composition comprises multiple thin nanosheets stacked in a three-dimensional (3D) nanoflower structure [14]. In_4SnS_8 monomer photocatalysts typically show low photocatalytic activity because of low space utilisation, insufficiently exposed active sites in the catalytic reaction and the poor separation and transport efficiency of photogenerated electron-hole pairs [15]. Therefore, the development of novel In_4SnS_8 catalytic structures is urgent.

Researchers have devised various strategies for photocatalyst modification, including metal deposition, elemental doping, semiconductor compounding and crystallographic surface engineering [9,14,15]. Among such strategies, heterojunction construction is one of the most effective methods for enhancing the photocatalytic activity. This is attributed to the accelerated separation and transport of photogenerated carriers owing to the formation of a built-in electric field at the interface of heterojunctions. Furthermore, two materials with matching energy bands can work synergistically to induce electron directional movement, thereby inhibiting the complexation of electron-hole pairs [16,17]. Perovskite quantum dots (QDs) with good photophysical properties show considerable potential in various applications, such as photodetectors, solar cells, light-emitting diodes, field-effect transistors, optical fibres and photocatalysts [18,19]. However, conventional lead-containing perovskite QDs are toxic and highly unstable [20,21], thus necessitating the development of new non-toxic lead-free perovskite QD materials.

This study employs an in situ assembly strategy for fabricating $\text{In}_4\text{SnS}_8/\text{Cs}_3\text{Bi}_2\text{Br}_9$ -X (ISS/CBB-X) photocatalysts by assembling lead-free perovskite $\text{Cs}_3\text{Bi}_2\text{Br}_9$ (CBB) QDs on In_4SnS_8 (ISS) nanoflowers. Experimental results show the high photocatalytic CO_2 reduction efficiency of the prepared ISS/CBB photocatalyst ($9.55 \mu\text{mol g}^{-1} \text{h}^{-1}$), 3.8 times higher than that of monolithic ISS materials. Based on the results of in situ X-ray photoelectron spectroscopy (XPS) and energy band structural analysis, step-scheme (S-scheme) heterojunction photocatalysts can be formed using ISS and CBB. Intriguingly, femtosecond transient absorption (fs-TA) spectroscopy as well as photoelectrochemical and photophysical tests revealed that the prepared composite photocatalysts effectively suppress the complexation of

electron-hole pairs and the carriers are effectively separated, yielding a high reduction potential. Moreover, the prepared ISS/CBB photocatalysts show high selectivity for CO_2 reduction products, achieving a CO selectivity of 92.9%. Finally, the effect of the composite materials on the formation of intermediates in the reaction is investigated using in situ diffuse reflectance infrared Fourier transform (DRIFT) spectroscopy and density functional theory (DFT) calculations.

2. Experimental

2.1. Chemicals and materials

Caesium bromide (CsBr ; 99.9%), bismuth tribromide (BiBr_3 ; 99%), octylamine (OLAm; 99.9%), dimethylsulfoxide (DMSO; analytical grade), oleic acid (OA; $\geq 90\%$), ethanol anhydrous (analytical grade), 3-mercaptopropionic acid (MPA; 99%) and ethylene glycol (analytical grade) were purchased from Sinopharm Chemical Reagent Co., Ltd, China. Silver nitrate (AgNO_3) was purchased from Sigma Aldrich. All chemicals were used without further purification.

2.2. Preparation of photocatalyst

2.2.1. Synthesis of $\text{Cs}_3\text{Bi}_2\text{Br}_9$ quantum dots

Typically, 1.28-g CsBr and 1.79-g BiBr_3 were accurately weighed and dissolved in 6-mL DMSO under continuous stirring conditions for 2 h. Then, 66- μL OLAm was added dropwise to this solution, achieving clear solution A. Next, 1 mL of solution A was slowly dropped into a mixture containing 10-mL ethanol and 1-mL OA, which was then heated to 80°C under vigorous stirring conditions; the resultant solution was labelled solution B. Finally, solution B was centrifuged at 8000 rpm for 10 min to remove large particles, affording homogeneous CBB QDs.

2.2.2. Synthesis of In_4SnS_8 nanoflowers and $\text{In}_4\text{SnS}_8/\text{Cs}_3\text{Bi}_2\text{Br}_9$ quantum dot systems

ISS/CBB was synthesised using a simple in situ hydrothermal method. First, 0.46 g of $\text{InCl}_3 \cdot 4\text{H}_2\text{O}$ and 0.14 g of $\text{SnCl}_4 \cdot 5\text{H}_2\text{O}$ were weighed and added to 80-mL H_2O under uniform stirring conditions. Then, the solution was treated with 0.4 g of L-cysteine and stirred until a clear and transparent solution was obtained. Thereafter, various amounts of CBB QD solutions were added dropwise to the solution. Further, ISS was prepared without adding the CBB QD solution.

Finally, the uniform solution was transferred to a 100-mL Teflon-lined hydrothermal autoclave, placed in a stainless steel sleeve and

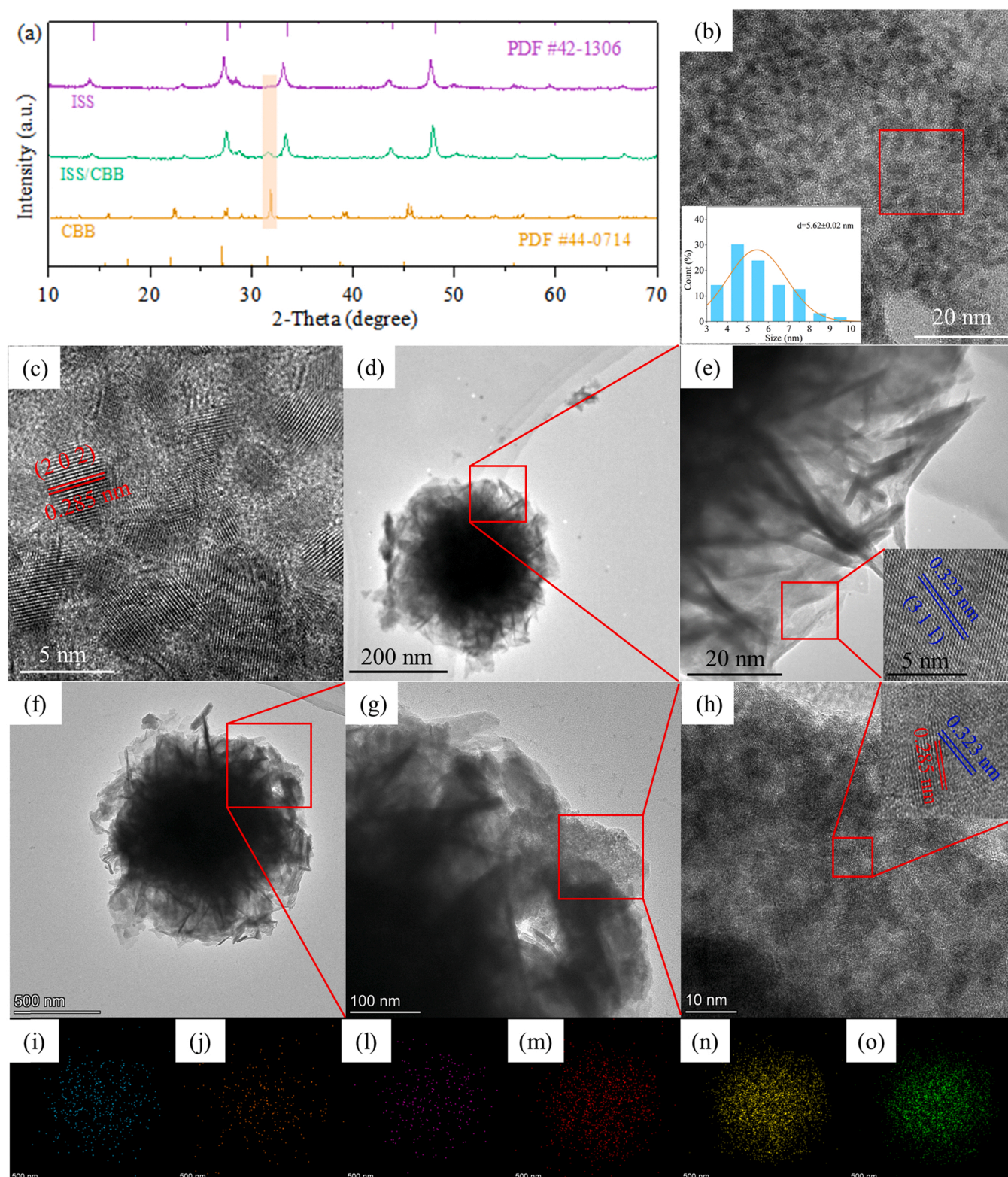


Fig. 2. (a) XRD patterns of catalysts; TEM and HR-TEM images of (b, c) CBB QDs, (inset of b) statistic size distribution, (d, e) ISS nanoflowers and (f-h) ISS/CBB heterojunction; (i-o) EDS elemental mapping of Cs, Bi, Br, In, Sn, S of ISS/CBB.

continuously heated at 160 °C for 24 h. After cooling to room temperature, the product was collected via centrifugation and washed three times with distilled water and ethanol each. The resultant products were dried in vacuum at 60 °C for 8 h and labelled ISS/CBB-0.5 (5% ISS QDs), ISS/CBB (10% ISS QDs), and ISS/CBB-1.5 (15% ISS QDs). The detailed preparation process is shown in Fig. 1.

2.3. Characterisation

The characterisation details of the samples are described in the [Supporting Information](#).

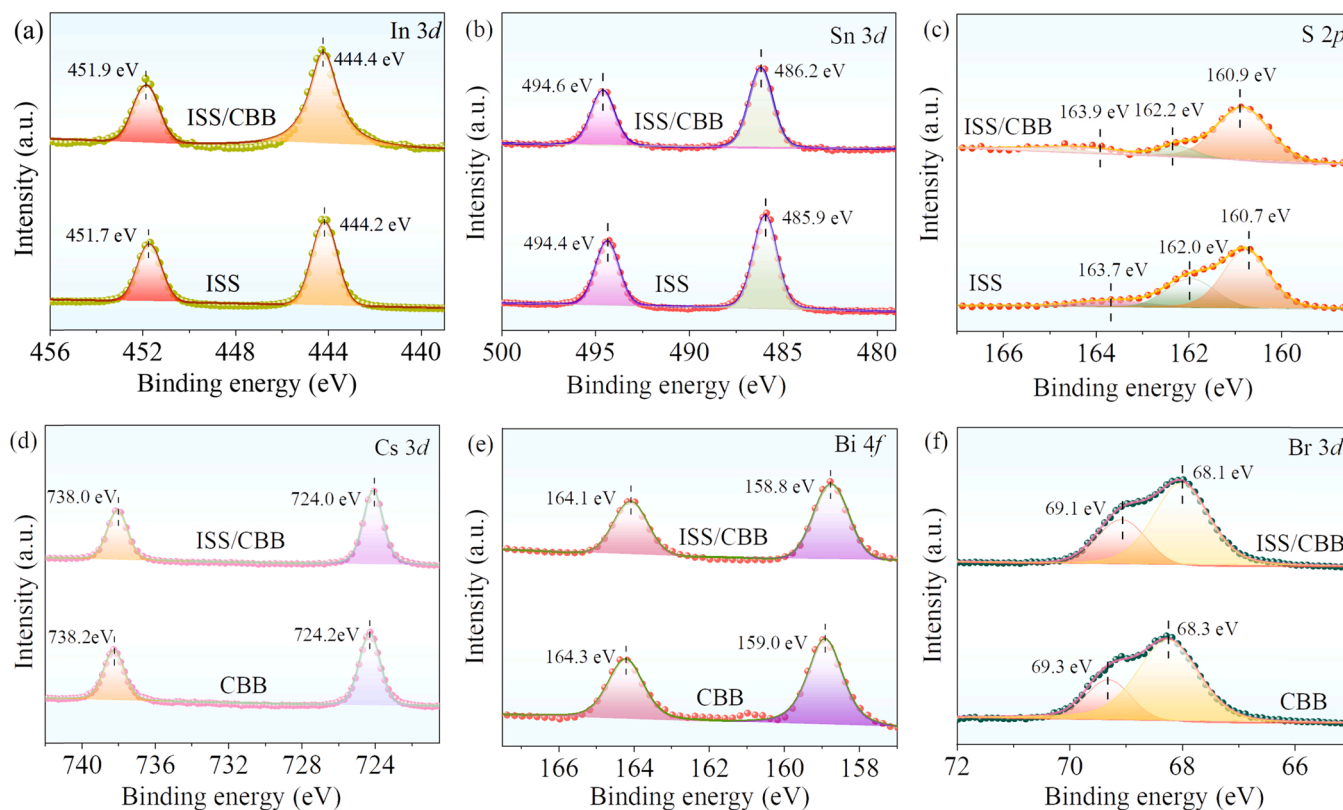


Fig. 3. (a–c) High resolution XPS spectra with peak for In 3d, Sn 3d and S 2p deconvolutions for ISS and ISS/CBB. (d–f) High resolution XPS spectra with peak for Cs 3d, Bi 4f and Br 3d deconvolutions for CBB and ISS/CBB.

2.4. Photocatalytic CO₂ reduction

First, 10 mg of the photocatalyst was dispersed in 2-mL deionised water and sonicated for 1 h, affording an orange suspension. This suspension was dropped onto a glass fibre filter paper, which was pre-treated at 400 °C for 6 h to remove any organic compound. The glass fibre filter paper was then dried for 4 h at 60 °C. The dried, dispersed glass fibre paper with the catalyst was placed in all glass automatic on-line trace gas analysis system (Labsolar-6A, Beijing Perfectlight) with the catalyst side facing upwards. Concurrently, 0.5 mL of deionised water was injected into the photocatalytic reactor. Second, the catalytic system was evacuated and injected with 99.999% pure CO₂ gas inside the vessel at 80 KPa. The CO₂-filled photocatalytic system was retained in the dark for 1 h before being exposed to light illumination to allow the catalyst to reach equilibrium for CO₂ adsorption. Finally, the catalyst was illuminated for 6 h using a 300-W argon lamp ($\lambda > 420$ nm). The CO₂ reduction products were detected using gas chromatography (GC; GC-2014 C). The CO selectivity was calculated using the formula CO selectivity (%) = $\frac{R_{CO}}{R_{CO} + R_{H_2}} \times 100\%$, where R_{CO} and R_{H_2} represent the production rates of CO and H₂, respectively.

The test procedure for the photocatalytic ¹³CO₂ reduction isotope experiment was the same as that for the standard photocatalytic CO₂ reduction test, except that ¹²CO₂ was replaced with ¹³CO₂ and the reduction products were tested using GC–mass spectrometry (MS) (GC model 6890 N/MS model 5973, Agilent Technologies).

2.5. Theoretical calculations

All the DFT calculations were performed on the Vienna Ab initio simulation package (VASP 5.4.4). The electron–ion interactions were investigated using the projector augmented-wave method, and the exchange–correlation energy was examined using the

Perdew–Burke–Ernzerhof functional method with generalised gradient approximation [22,23]. The plane wave cut-off energy was set to 450 eV. All the structures were fully relaxed until the atom force was < 0.02 eV Å^{−1}. The energy barrier of the C–C coupling process was estimated using the climbing image nudged elastic band (CI-NEB) method [22]. Based on the Monkhorst–Pack scheme, Brillouin-zone sampling was performed using a $4 \times 2 \times 1$ k mesh. Detailed parameters of the Gibbs free energy calculations are described in the Supporting Information.

3. Results and discussion

3.1. Characterisation of In₄SnS₈/Cs₃Bi₂Br₉ heterojunction

Fig. 2a shows the X-ray diffraction (XRD) spectra of the pristine ISS, CBB and ISS/CBB composites. The sharp XRD peaks of the CBB composite at 22.2°, 27.2°, 31.7° and 45.3° corresponded to the (102), (003), (202) and (204) planes and matched well with the characteristic peaks of CBB (JCPDS No. 44–0714) [24,25]. For pristine ISS, considerable XRD peaks were detected at 27.7°, 33.6°, 44.0° and 48.2°, attributed to the (311), (400), (333) and (440) planes of ISS (JCPDS No. 42–1306), respectively [14]. Note that the characteristic XRD peaks of both CBB and ISS could be detected in the ISS/CBB-X composite samples with some offset, and no other new peaks were observed, demonstrating the successful synthesis of the ISS/CBB composites.

The prepared CBB QDs showed high dispersion with a spherical particle shape (Fig. 2b and c). Interestingly, the diameter distribution of CBB QDs was relatively uniform, with a mean diameter of 5.6 nm. Furthermore, the prepared ISS exhibited a 3D nanoflower structure, formed by the accumulation of ultrathin nanosheets with individual layers of 2–4 nm (Fig. 2d and e), which facilitated electron transfer [15]. The incident light would be reflected several times when it hits the interior of the nanoflower, thus ensuring the complete utilisation of the

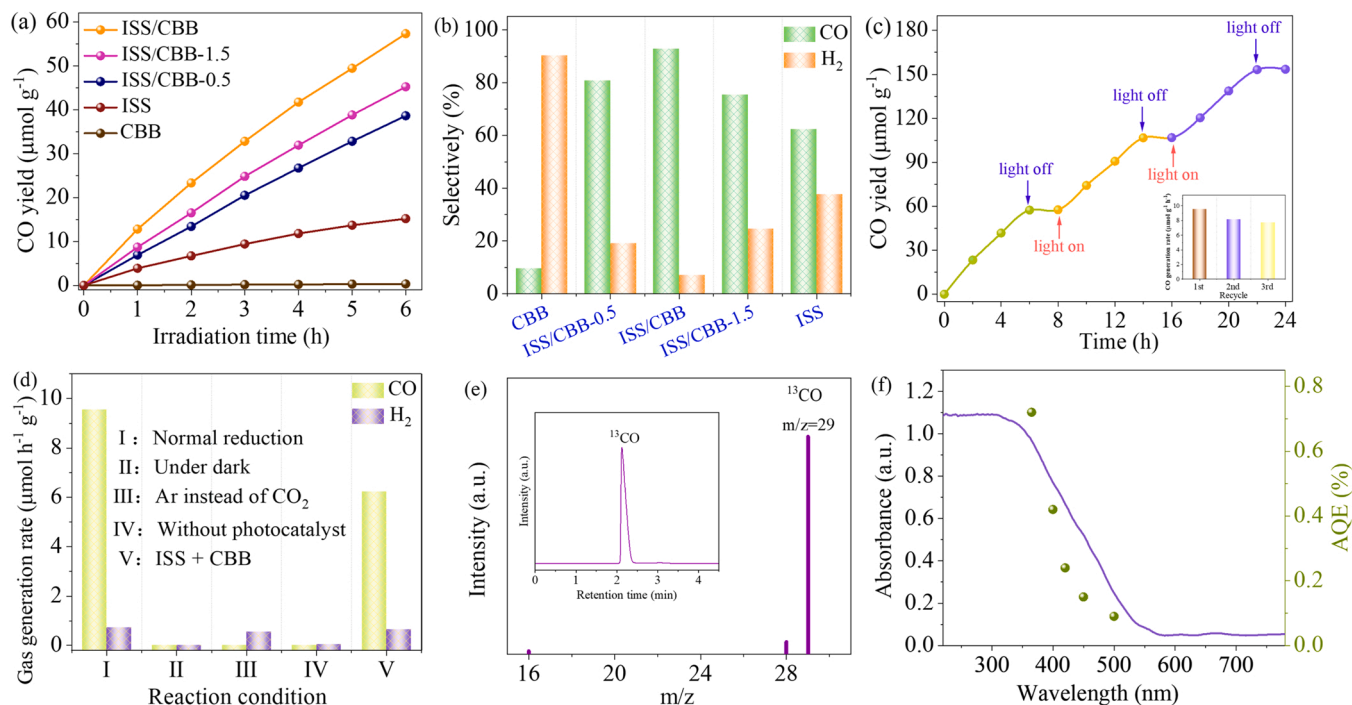


Fig. 4. (a) CO yield as a function of irradiation time and (b) H₂ and CO selectivity at irradiation time 6 h for CBB, ISS, ISS/CBB-0.5, ISS/CBB-1.5 and ISS/CBB; (c) The recycle activity of ISS/CBB for the photocatalytic CO₂ reduction; (d) Evolution of CO and H₂ under different reaction conditions; (e) The GC-MS analysis for CO produced from ¹³CO₂ isotope experiment, (inset of e) the gas chromatogram of ¹³CO; (f) Wavelength-dependent AQE of CO₂ reduction to CO on ISS/CBB.

incident light [26]. Compared with the smooth edges of pristine ISS, the edges of ISS/CBB exhibited a rough texture, indicating the successful anchoring of the CBB QDs to the ISS surface. The high-resolution transmission electron microscopic images reveal an interface between the ISS and the CBB QDs (Fig. 2f–h), indicating the embedding of the CBB QDs into the ISS surface.

For ISS/CBB, the lattice spacings of 0.323 and 0.285 nm corresponded to those between the ISS (311) and CBB QD (202) crystal planes, consistent with the XRD results [14,25]. Fig. 2i–o present the elemental mapping of the ISS/CBB composite, showing the uniform distribution of individual elements, indicating the successful synthesis of ISS/CBB. The contents of In, Sn and S were considerably higher than those of Cs, Bi and Br, consistent with the experimental results.

Based on energy dispersive spectrometric analysis, the CBB QD content was 10% (Fig. S1 and Table S1), corresponding to the experimental results. The full spectra of ISS, CBB and ISS/CBB in Fig. S2 shows the relevant characteristic peaks that represented In, Sn, S, Cs, Bi and Br, thus confirming the synthesis of high-purity ISS, CBB and ISS/CBB photocatalysts. Two distinctive peaks appeared at bond energies 444.2 and 451.7 eV in the case of ISS and at 444.4 and 451.9 eV in the case of ISS/CBB, attributed to In 3d_{5/2} and 3d_{3/2}, respectively, indicating the presence of In³⁺ in the samples (Fig. 3a) [15]. In Fig. 3b, the bond energies at 485.9 and 486.2 eV for ISS and 494.4 and 494.6 eV for ISS/CBB corresponded to Sn 3d_{5/2} and Sn 3d_{3/2}, respectively, indicating the Sn⁴⁺ oxidation state of Sn in the samples [14]. The 2p peak of S can be divided into three peaks at 160.7, 162.0 and 163.7 eV (Fig. 3c), suggesting the presence of S in the sulphide phase [27]. In particular, compared with ISS, the binding energy of the atoms in ISS/CBB showed a 0.2 eV positive shift, suggesting the potential considerable transfer of electrons from ISS to CBB in ISS/CBB [28,29].

Fig. 3d–f show the XPS images of CBB and ISS/CBB. For the CBB sample, two considerable peaks of Cs 3d were detected at 738.2 and 724.2 eV, representing 3d_{3/2} and 3d_{5/2}, respectively [30]. For the CBB sample, the characteristic peaks of Bi 4f (164.3 and 159.0 eV) and Br 3d (69.3 and 68.3 eV) matched those reported in the literature [31], indicating the successful preparation of CBB. For the ISS/CBB sample, the

XPS characteristic peaks of Cs 3d, Bi 4f and Br 3d showed a 0.2 eV shift towards the lower binding energy compared with CBB, further suggesting that electrons would be transferred from ISS to CBB in ISS/CBB.

3.2. Photocatalytic CO₂ activity of samples

The photocatalytic CO₂ reduction activity of the samples was tested in a closed system using a 300-W xenon lamp as the light source. After 6 h of illumination, ISS achieved a CO yield of 15.2 μmol/g (Fig. 4a). However, no CO₂ reduction product was detected in the CBB catalytic system, which may be ascribed to the high conduction band (CB) of CBB that failed to meet the thermodynamic conditions for CO₂ reduction [20]. Notably, ISS/CBB achieved a CO yield of 57.3 μmol/g, 3.8 times higher than that achieved using ISS. Moreover, increasing the ISS content to 15% slightly reduced the photocatalytic CO₂ reduction activity of the composite (ISS/CBB-1.5), achieving a CO yield of 45.2 μmol/g after 6 h of light illumination.

ISS and ISS/CBB showed CO selectivities CO of 53.4% and 92.9%, respectively (Fig. 4b). The heterojunction photocatalyst exhibited good CO selectivity and effectively enhanced overall photocatalytic activity. Fig. 4c shows the rate plots of the optimal-activity ISS/CBB sample for three consecutive reaction cycles. Under light illumination, the CO production rates remained relatively constant. Intriguingly, the XRD spectra and scanning electron microscopic images of ISS/CBB before and after the reaction were nearly identical (Fig. S3). Furthermore, it can be seen that the content and binding energy position of the element in the ISS/CBB have not changed after the cycling experiment in Fig. S4 and Table S2, which indicates the high stability of the photocatalytic material [32,33].

To investigate influencing factors in the experiments, a series of condition-controlled experiments was conducted. Under dark conditions, almost no products were detected, confirming the importance of light in the reaction process (Fig. 4d). Moreover, the experiments were conducted using Ar instead of CO₂; the results showed that neither the production of CO nor H₂. Thus, the C in the product could be attributed to the reduced CO₂ [34]. For the experiments performed on the control

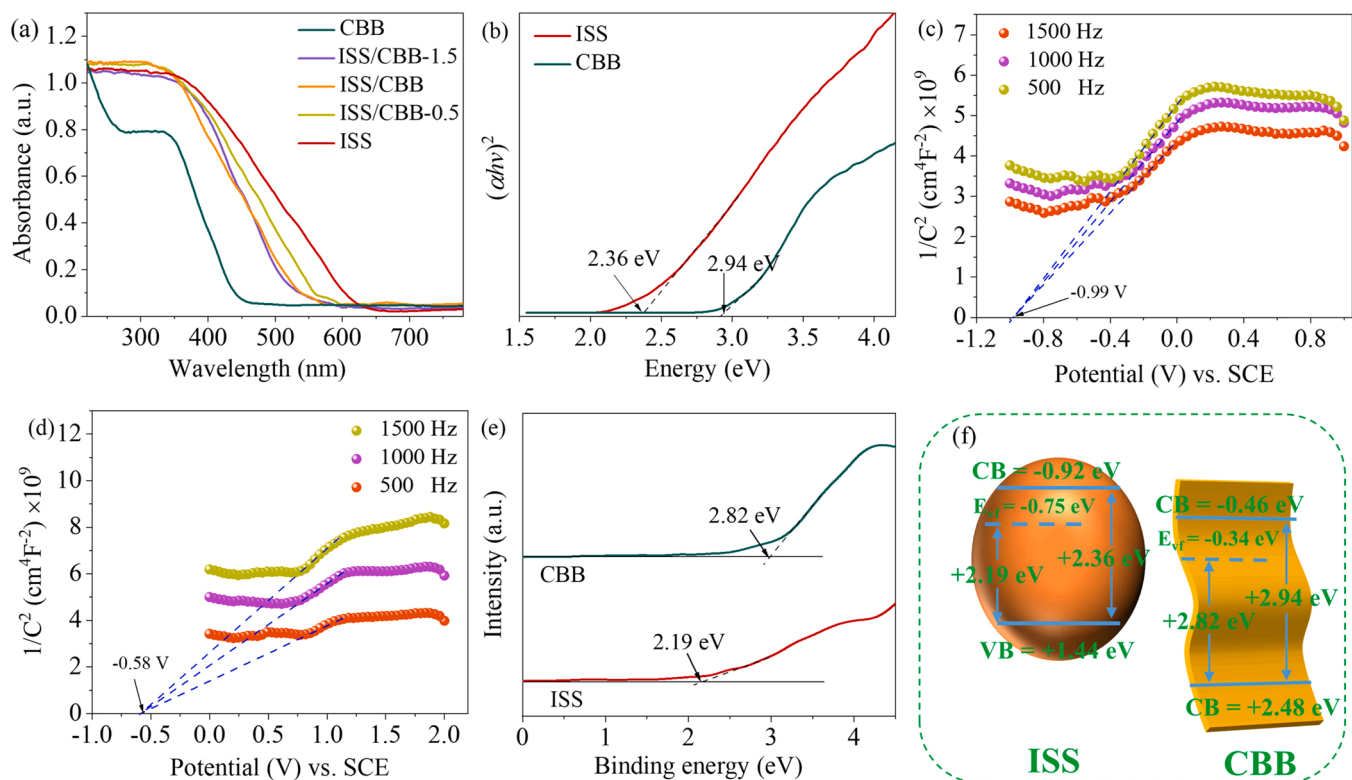


Fig. 5. (a) UV-vis diffuse reflection spectra of photocatalysts; (b) the estimated band gaps; (c, d) the Mott-Schottky plots at 500, 1000 and 1500 Hz of ISS and CBB; (e) XPS valence band spectra and (f) Schematic energy-band diagram of ISS and CBB.

group without adding a catalyst, no CO product was obtained, indicating that the catalyst is essential to obtain CO and serves as the driving force for the reaction [35]. The activity of the mechanical mixing of ISS and CBB as a catalyst was tested, and the CO production rate was only 6.23 $\mu\text{mol g}^{-1} \text{h}^{-1}$, which considerably differed from the activity of the

ISS/CBB heterojunction, thereby confirming that the heterojunction material was not formed via a simple physical coacervation between ISS and CBB [36].

Isotopic measurements were performed using $^{13}\text{CO}_2$ as the reaction gas source for analysing CO production and further investigating the

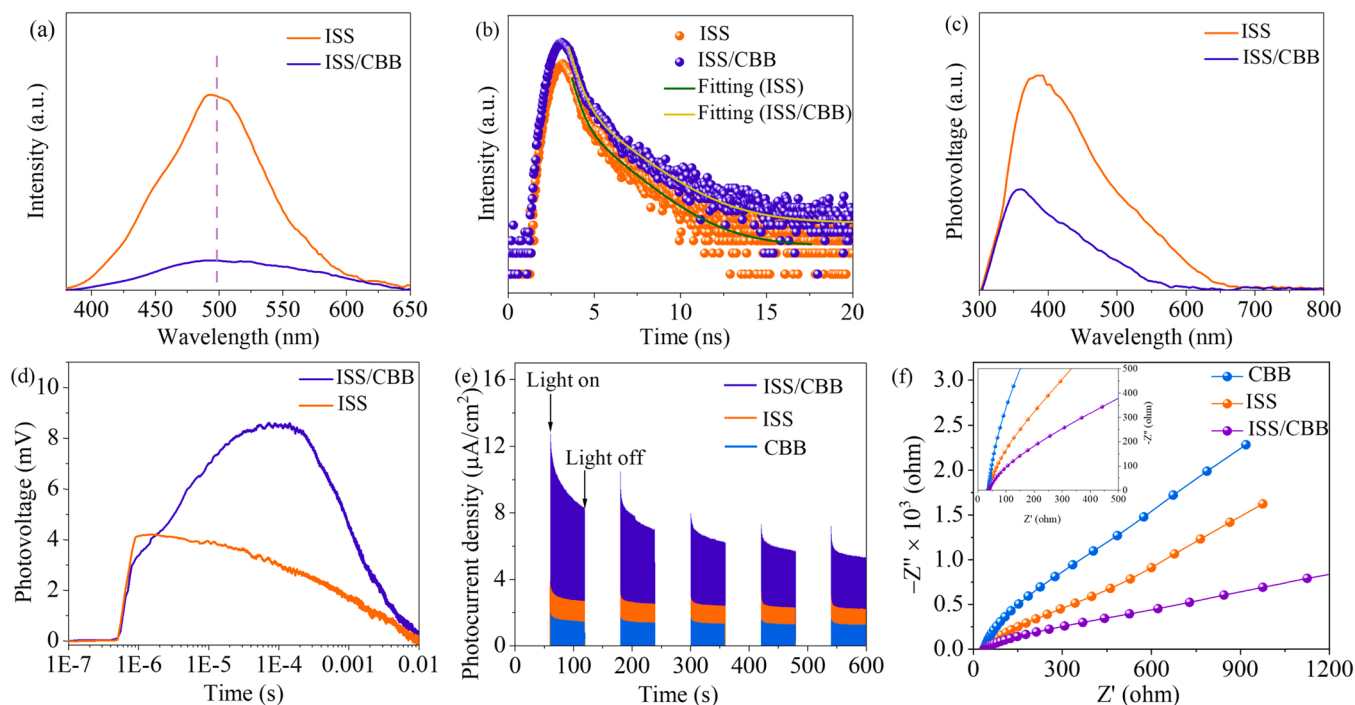


Fig. 6. (a) Photoluminescence (PL) spectra, (b) TR-PL spectra with corresponding fitting results, (c) surface photovoltage spectra (SPV), (d) transient photovoltage spectra (TPV) of the as-prepared ISS and ISS/CBB composites; (e) Transient photo-current responses, (f) EIS spectra of CBB, ISS and ISS/CBB.

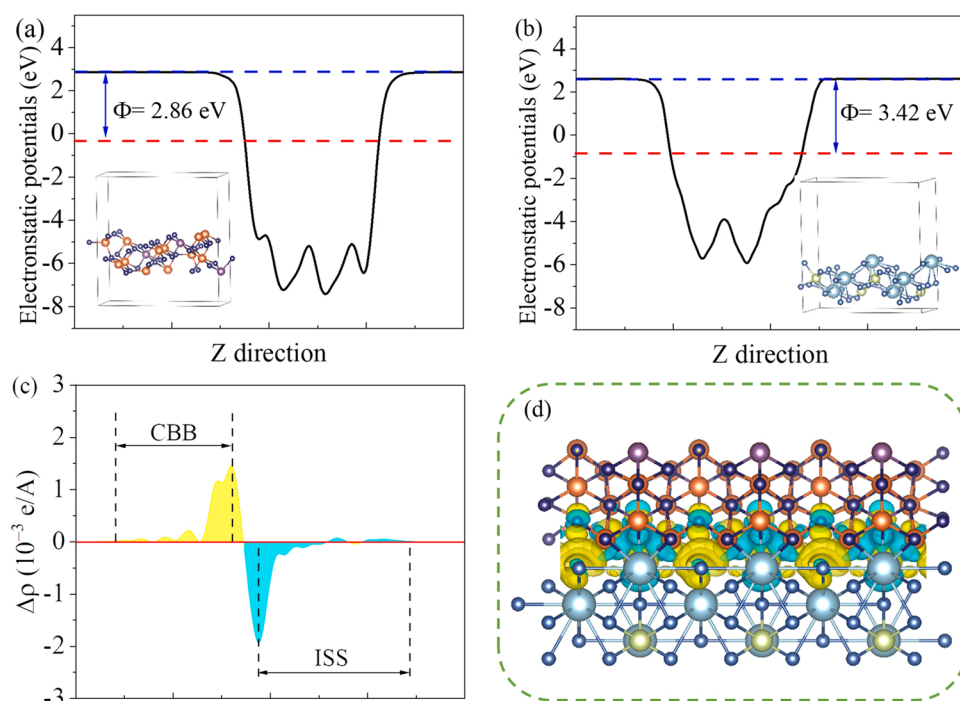


Fig. 7. (a) The calculated work function of ISS, (inset of a) structural model of the (1 0 1) plane; (b) the calculated work function of CBB, (inset of b) structural model of (0 0 1) plane; (c) The planar-averaged electron density difference of ISS/CBB heterojunction; (d) side view of the charge density difference over the ISS/CBB heterojunction. (The yellow and cyan areas represent accumulation and depletion of electrons, respectively). (For interpretation of the references to colour in this figure legend, the reader is referred to the web version of this article.)

actual source of the reduction products. The photocatalytic process afforded ^{13}CO as a product (Fig. 4e), indicating that CO_2 was the primary C source. Furthermore, the apparent quantum efficiency (AQE) of the prepared ISS/CBB for CO generation was calculated to be 0.24% at 420 nm (Fig. 4f). Interestingly, the AQE trend showed a good fit with the light absorption spectra of the ISS/CBB photocatalysts, thus presenting strong evidence for CO_2 photoreduction to CO [22].

3.3. Effective separation of carriers

The adsorption bands of ISS and CBB were detected at 620 and 450 nm (Fig. 5a), respectively, showing a strong response in the visible regions. After the introduction of CBB, the light absorption capacity of ISS/CBB-X was between ISS and CBB. With increasing CBB loading, the light absorption performance of ISS/CBB-1.5 weakened and the ultraviolet (UV) absorption edge showed a blue shift in the ISS/CBB-X series. Moreover, compared with pristine CBB, ISS/CBB showed a broad light absorption range and high utilisation of visible light. The sample bandwidths were estimated using the Kubelka–Munk (KM) equation and by the linear fitting of the KM function to the energy axis [37,38]. The ISS and CBB bandwidths were calculated to be 2.36 and 2.94 eV, respectively (Fig. 5b).

The CB and valence band (VB) positions of ISS and CBB were examined to further investigate the mechanism of photogenerated carriers. The Mott–Schottky plots at frequencies of 500, 1000 and 1500 Hz were used to estimate the flat-band potentials of ISS and CBB. The slope of the MS curve was positive in the case of both ISS and CBB (Fig. 5c and d), indicating both materials as n-type semiconductors [39,40]. Thus, the flat-band potential was consistent with the Fermi energy level. The flat-band potentials (vs. saturated calomel electrode; pH = 7) of ISS and CBB were calculated to be -0.99 and -0.58 V, respectively, which were -0.75 and -0.34 eV when converted to a normal hydrogen electrode (NHE; pH = 7). Furthermore, based on the VB XPS spectra of ISS and CBB (Fig. 5e), VB maximum values of 2.19 and 2.82 eV, respectively, were achieved, indicating values between the Fermi level and VB. Accordingly, the CB positions of ISS and CBB were -0.92 and -0.46 eV, respectively. Fig. 5f shows a detailed bandgap structure.

The effective separation of photogenerated electron–hole pairs is an

efficient approach for improving the photocatalytic performance. The complexation of electron–hole pairs can be observed using photoluminescence (PL) spectra. When the emission intensity is low, a decreased rate of recombination of the photogenerated electron–hole pairs and efficient separation of the electron–hole are achieved [41,42]. A broad fluorescence peak at ~ 500 nm was observed in the cases of ISS and ISS/CBB, and the fluorescence intensity of ISS/CBB reduced compared with that of the original ISS, indicating that the electron–hole pairs were effectively separated (Fig. 6a).

The photogenerated charge is a key factor in photocatalytic CO_2 reduction, and the lifetime of this charge can provide a better understanding of the photocatalytic reaction mechanism. When the photogenerated carrier lifetime is long, the photogenerated electrons and holes have more time to migrate to the active sites on the catalyst surface and participate in the photocatalytic reaction, thereby increasing the photocatalytic activity of the material [43].

Time-resolved photoluminescence (TR-PL) spectroscopy was performed on the ISS and ISS/CBB catalysts (Fig. 6b), and the double exponential function was employed to fit the fluorescence lifetime (Table S3). The fluorescence lifetime of the ISS catalyst was only 2.76 ns. Alternatively, after the CBB modification of ISS (ISS/CBB heterojunction), the average photogenerated charge lifetime was 4.87 ns, indicating that the photogenerated carriers in the ISS/CBB catalyst require a longer time to perform the CO_2 photoreaction on the catalyst surface and enhance the catalytic activity [44].

Using the surface photovoltage (SPV) technique, the separation characteristics of the photogenerated carriers can be accurately and efficiently reflected, revealing their separation efficiency and transfer direction [45,46]. Generally, a positive signal indicates that the holes are transferred to the light-receiving side of the photocatalyst. Conversely, a negative signal indicates that electrons are transferred to the light-receiving side of photocatalysts. As shown in Fig. 6c, the pristine ISS photocatalyst exhibited a strong positive SPV response at 300–650 nm, potentially attributed to the bandgap transition of ISS. Surprisingly, the ISS/CBB catalyst showed a weaker SPV response signal than the ISS catalysts, implying that more electrons were transmitted to the surface. Notably, the SPV signal dynamics of ISS and ISS/CBB suggest that the CB photoelectrons of CBB may transfer to the ISS surface

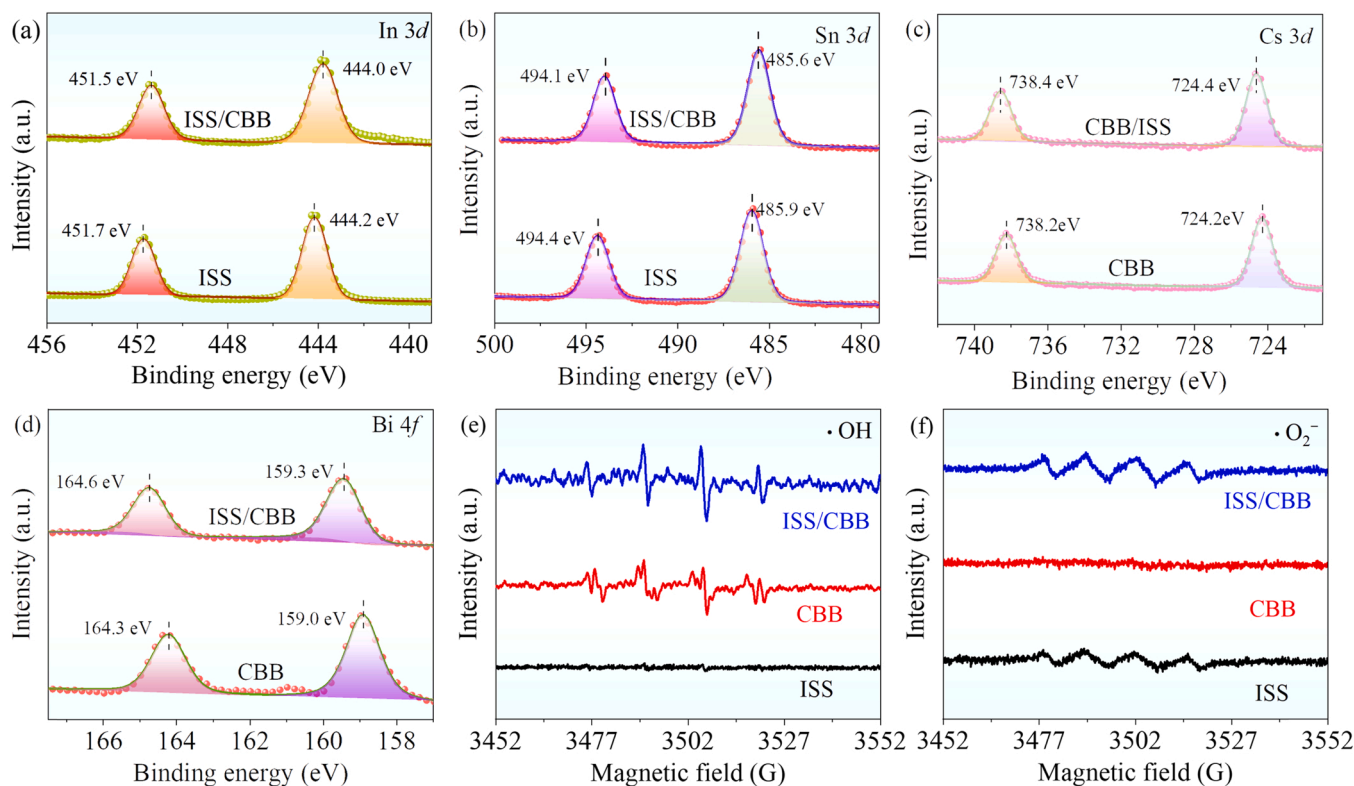


Fig. 8. High-resolution XPS spectra of (a) In 3d and (b) Sn 3d for pure ISS and ISS/CBB tested under illumination; XPS spectra of (c) Cs 3d and (d) Bi 4f of pristine CBB and ISS/CBB tested under illumination; ESR signals of (e) DMPO-•OH adducts in water and (f) DMPO-•O₂⁻ adducts in methanol over CBB, ISS and ISS/CBB photocatalysts under illumination.

and recombine with the VB holes.

The signal strength of the transient photovoltage spectrum can be used to describe the separation of photogenerated electron-hole pairs. Moreover, when the TR-SPV signal is intense, the charge separation is enhanced [47,48]. Under N₂ conditions, the ISS and ISS/CBB samples were tested for TR-SPV to further reveal the charge separation of the samples. The TR-SPV pattern of the sample excited using a laser with a 10-ns pulse width and a 355-nm wavelength is shown in Fig. 6d. The test results show that the ISS/CBB sample exhibited an intense TR-SPS signal, indicating that the charge separation of ISS/CBB improved considerably and the lifetime of the photogenerated carriers increased substantially. This result reflects the considerable photocatalytic activity of the ISS/CBB photocatalyst, consistent with the results of the PL and TR-PL spectroscopy.

Photoelectric-chemical tests were performed to investigate the carrier separation performance of the photocatalytic materials. Fig. 6e shows the intensity of the transient photocurrent response curve of the samples under visible light irradiation. The photocurrent responses of ISS and CBB were weak; however, the intensity of the photogenerated current increased for ISS/CBB, indicating that the effective separation of the photogenerated electron-hole pairs in ISS/CBB [11,26].

In the absence of light, the electrochemical impedance spectrum (EIS) was evaluated to determine the photogenerated carrier transport resistance. The diameter of the Nyquist plot (Fig. 6f) reflects the magnitude of the carrier transport resistance at the working electrode. Generally, when the electron transport resistance is low, the diameter of the semicircle in the EIS is small [14,22]. Compared with the original ISS and CBB, ISS/CBB showed the smallest diameter in the EIS, indicating its lowest resistance to electron transport. Based on the aforementioned results, ISS/CBB exhibits a more efficient separation of photogenerated carriers relative to ISS and CBB.

3.4. S-scheme carrier transfer pathway

DFT analysis was performed to understand the carrier transfer pathway and evaluate the electronic properties of the photocatalytic materials. The bandgaps were determined to be 1.37 and 2.49 eV for ISS and CBB (Fig. S5), respectively, consistent with the experimental results. Furthermore, the calculated work functions for ISS and CBB were 2.86 and 3.42 eV, respectively (Fig. 7a and b). Therefore, when the two photocatalysts were combined, the difference in the Fermi energy level promoted the transfer of electrons from ISS to CBB until the Fermi energy level reached equilibrium [23,28,49].

The difference in the charge density between the ISS and CBB can visually reflect the carrier transfer. The yellow and marine green colours in Fig. 7c and d represent charge accumulation and loss, respectively. In the ISS/CBB heterojunction, the carriers could spontaneously transfer from the ISS to the CBB layer. Consequently, charge accumulation occurred on the CBB layer, whereas charge loss was observed on the ISS layer. Thus, a strong electric field was formed between the two semiconductor materials, facilitating carrier transfer between the photocatalysts.

To the best of our knowledge, the VB electrons of ISS and CBB both jumped to their CBs under light illumination. The positive and negative shifts of the binding energy indicated a decrease and increase in the electron density, respectively. Thus, the carrier transfer between the ISS and CBB interfaces in photocatalytic CO₂ reduction was further investigated using in situ irradiated (ISI) XPS. Fig. 8a–d show changes in the binding energies of In, Sn, Cs and Bi in ISI-XPS tests performed under light and dark conditions. Compared with ISS, the characteristic peaks of the In 3d and Sn 3d orbitals in ISS/CBB shifted slightly towards the decreasing binding energy under light conditions, increasing the outer electron density of ISS in ISS/CBB (Fig. 8a and b). Moreover, the characteristic peaks of the Cs 3d and Bi 4f orbitals in ISS/CBB shifted slightly towards the high binding energy under light conditions, suggesting an

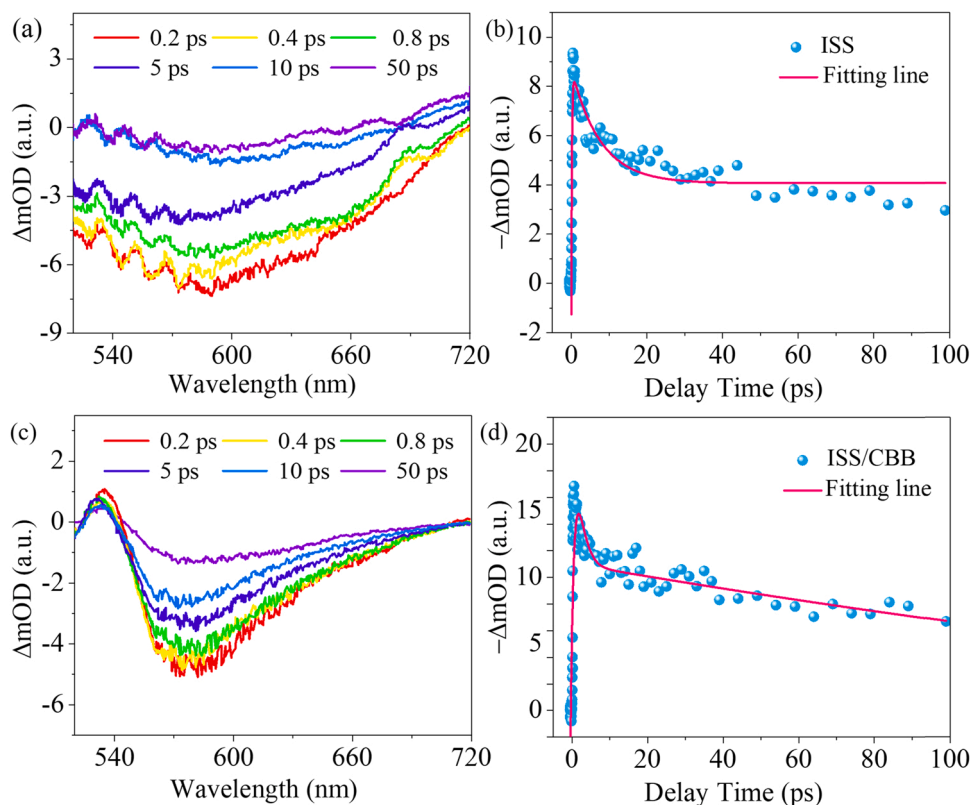
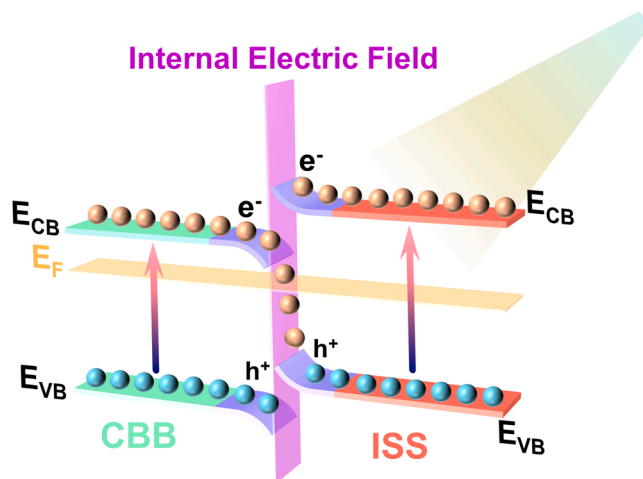


Fig. 9. (a) The fs-TA spectra of ISS and (b) experimental decay kinetics monitored under 620 nm; (c) the fs-TA spectra of CBB and (d) experimental decay kinetics fitted under 560 nm.

electron outflow from CBB to ISS in ISS/CBB (Fig. 8c and d). The change in the element binding energy directly reflects the direction of electron migration during the photocatalytic CO_2 reaction; thus, the electrons were transferred from CBB to ISS under light conditions, opposite to the electron transfer trend observed under dark conditions [28,40].

To further investigate the enhanced photocatalytic CO_2 reduction activity of the ISS/CBB composite and detect superoxide radicals ($\cdot\text{O}_2^-$) and hydroxyl radicals ($\cdot\text{OH}$) in the reaction system. Fig. 8e and f show the ESR spectra of the pristine ISS and CBB photocatalytic materials. For the ISS photocatalyst, four characteristic peaks with an intensity ratio of 1:1:1:1 were observed in a methanol solution, attributed to the $\text{DMPO}-\text{O}_2^-$ signal [50]; alternatively, no characteristic peak was detected in an aqueous solution. For pristine CBB, four characteristic peaks with an intensity ratio of 1:2:2:1 were observed in the aqueous solution, attributed to the $\text{DMPO}-\text{OH}$ signal [37]; however, no ESR signal was detected in a methanol solution. For ISS/CBB, four peaks with intensity ratios of 1:1:1:1 and 1:2:2:1 were detected, indicating that the ISS/CBB composite could yield both $\cdot\text{O}_2^-$ and $\cdot\text{OH}$ under light conditions. Based on radical trapping experiments and potential analysis, the ISS/CBB heterojunctions followed the S-scheme mechanism, consistent with the ISI-XPS results.

Further, fs-TA spectroscopy was performed to further investigate the separation of electron-hole pairs and elucidate the efficient interfacial charge transfer of ISS/CBB to determine the carrier transfer pathways in the composites. The bandgaps of ISS and CBB showed that they could be simultaneously excited at 400 nm. Thus, the excitation light of 400 nm (3.1 eV) was adopted for the fs-TA spectroscopic measurements. Both ISS and ISS/CBB exhibited a broad negative absorption band (Fig. 9a and c), primarily attributed to the stimulated emission and photobleaching-state filling [51,52]. Moreover, the absorption band edges of ISS and ISS/CBB were 620 and 560 nm, respectively, consistent with the results of the UV-visible absorption spectroscopy. Compared with the original ISS photocatalyst, the ISS/CBB photocatalyst exhibited



Scheme 1. The S-scheme transfer mechanism of photogenerated electrons between CBB and ISS over ISS/CBB heterojunction under the visible light.

increased new positive absorption band, which may be related to the combination of holes and electrons on the ISS and CBB surfaces, respectively, at their interface. Moreover, compared with ISS, the negative absorption band of ISS/CBB became weaker, indicating a reduction in the holes on the ISS surface of ISS/CBB. These results conformed to an S-scheme transfer mechanism [43,51].

To evaluate the decay kinetics of the carrier, the time profiles of the TAS at 620 nm (ISS) and 560 nm (ISS/CBB) were fitted using a double exponential function (Fig. 9b and d); the corresponding fit parameters are listed in Table S4. Generally, short and long lifetimes (τ_1 and τ_2 , respectively) reflect the shallow and deep trapings of holes before

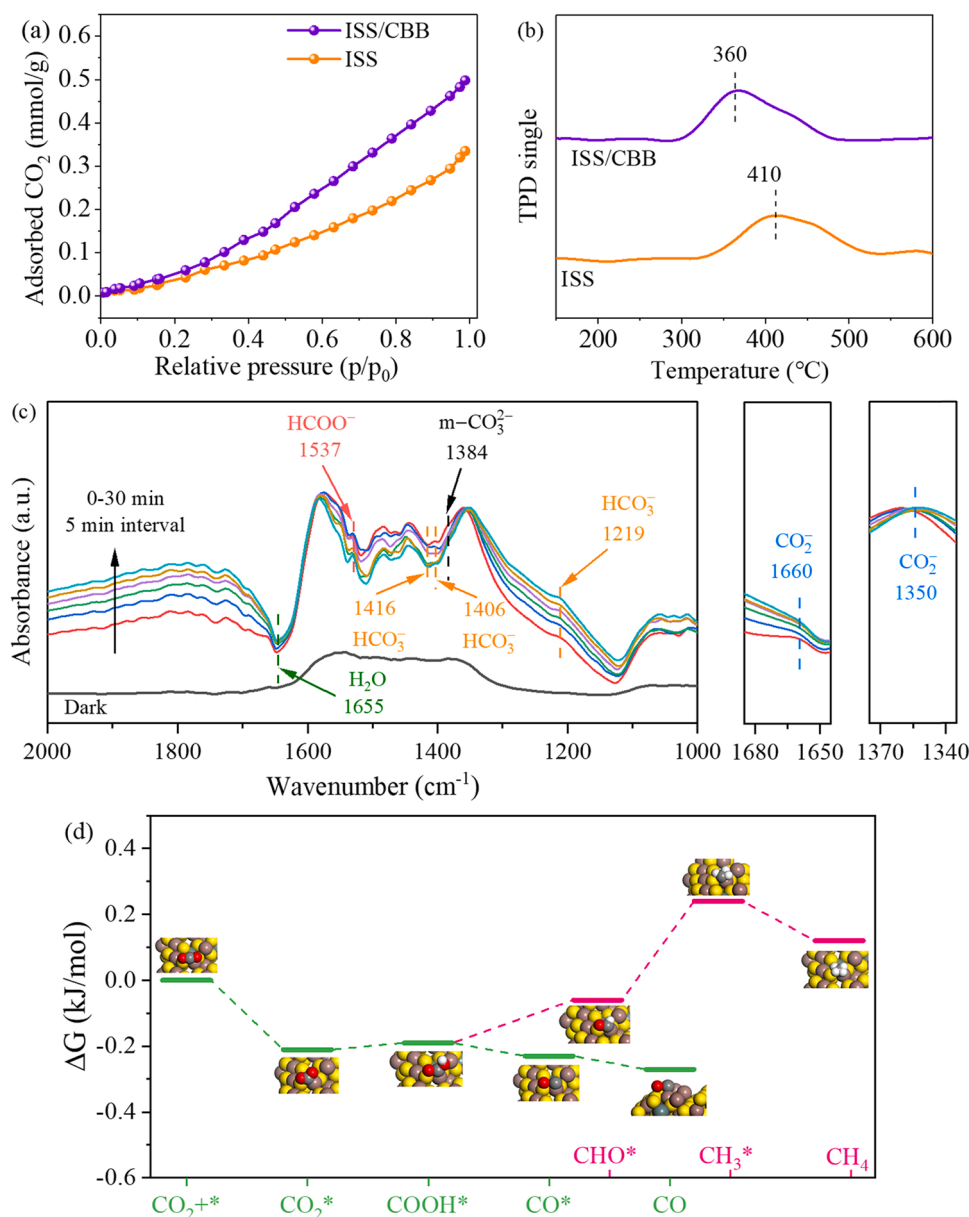


Fig. 10. (a) CO₂ adsorption isotherm, (b) CO-TPD curves for ISS and ISS/CBB samples; (c) In situ DRIFT profiles for CO₂ photoreduction over ISS/CBB; (d) Energy profile for the elementary steps of CO₂ reduction to CO and CH₄ over (1 0 1) facets of ISS.

electron-hole recombination, respectively. The shallow and deep hole-trapping time constants for the pure ISS photocatalyst were 21.47 and 320.21 ps, respectively. However, the decay lifetimes of the ISS/CBB nanomaterials were 1.32 and 25.16 ps, suggesting strong shallow electron trapping and effective electron transfer, which can improve the CO₂ reduction performance [22,52]. Moreover, the prolonged lifetime of the active species ($\tau_3 = 493.1$ ps) of ISS/CBB may be associated with the shallow trapping of electron-hole recombination. The pseudo-colour TA plots of ISS and ISS/CBB under 400-nm fs excitation with a ~ 0.8 -mJ fluence at a 1-kHz repetition rate is shown in Fig. S6.

Based on the aforementioned analysis, Scheme 1 depicts the carrier transfer method in the ISS/CBB composites, compatible with the S-scheme heterojunctions. Under light conditions, the built-in electric field of the ISS/CBB heterojunction promoted carrier transfer from the VB of the ISS layer to the CB of the CBB layer. Furthermore, the built-in electric field would prevent reverse carrier movement, which could hinder the transfer of photogenerated electrons from the CB of the ISS layer to the CB of the CBB layer [28,38]. Accordingly, the transfer of

holes generated from the VB of the ISS layer to the VB of the CBB layer was inhibited, promoting the participation of the photogenerated electrons and holes in the photocatalytic reaction and thus improving the photocatalytic performance. Thus, the S-scheme-based ISS/CBB heterojunction showed considerably improved photocatalytic quantum efficiency.

3.5. Selectivity of CO₂ reduction products

First, the CO₂ adsorption capacity of the ISS and ISS/CBB photocatalysts was analysed to gain insights into CO₂ adsorption and reduction processes. Fig. 10a presents the CO₂ adsorption isotherms of ISS and ISS/CBB, indicating that ISS/CBB exhibited better CO₂ absorption performance, thus facilitating CO₂ reduction.

Furthermore, in situ DRIFT spectroscopy was used to identify the intermediates formed during the ISS/CBB photocatalytic CO₂ reaction (Fig. 10c). After the exposure of ISS/CBB to a CO₂/H₂O gas mixture to reach adsorption equilibrium, the light was irradiated for 120 min and

the DRIFT spectra were collected every 5 min. The intensity of the CO_2^- (1660 and 1350 cm^{-1}) substance absorption peak on the ISS/CBB catalyst increased under illumination, suggesting that light facilitated the production of CO_2^- on the catalyst surface [46]. The intensity of HCO_3^- (1219, 1406 and 1416 cm^{-1}) increased slightly, while that of m-CO_3^{2-} (1384 cm^{-1}) decreased considerably, suggesting that the m-CO_3^{2-} species may be involved in the CO_2 reduction reaction through the formation of an HCO_3^- intermediate [22,29]. CO_2^- is regarded as a critical intermediate in CO_2 reduction, where the rate of CO_2^- formation is regarded as a critical step in photocatalytic CO_2 reduction. Theoretically, the energy barrier for HCO_3^- conversion to CO_2^- is $\sim 0.27\text{ eV}$ (vs. NHE), while that for linear CO_2 conversion to CO_2^- is approximately -1.9 eV (vs. NHE) [53]. Because of the modification of CBB on the ISS surface, the formation of HCO_3^- became more accessible, the energy barrier decreased and the CO_2 reduction activity increased. Interestingly, an absorption peak can be detected at 1537 cm^{-1} , possibly attributed to the vibration of HCOO^- , which was identified as a key intermediate in the formation of CO. Fig. 10b depicts the CO-TPD test for the ISS and ISS/CBB photocatalysts. Compared with ISS, the ISS/CBB photocatalyst showed a relatively low CO desorption temperature (360°C), implying that the generated CO would be easily released [22].

DFT calculations were applied to further understand the high selectivity of ISS/CBB photocatalysts for CO production at the atomic level. Four intermediate products, namely, CHO^* , COOH^* , CO^* and CH_3^* , can be produced during the formation of CO and CH_4 via photocatalyst CO_2 reduction [54]. The formation of the adsorbed COOH^* was the highest energy-barrier step in the CO generation process (Fig. 10d), and the subsequent transition from COOH^* to CO^* is expected to occur spontaneously. However, because the formation of CHO^* and CH_3^* is an endothermic process, the generation of CH_4 was limited in the photocatalytic CO_2 reduction process. Thus, the ISS/CBB photocatalysis achieves high CO selectivity.

4. Conclusions

The prepared innovative S-scheme-based ISS/CBB-X photocatalyst has shown outstanding results in terms of effective charge separation by adjusting the interfacial electric field. Impressively, the optimised ISS/CBB photocatalyst exhibits good activity and CO selectivity with a CO yield and selectivity of $9.55\text{ }\mu\text{mol g}^{-1}\text{ h}^{-1}$ and 92.9%, respectively, 3.8 and 1.5 times higher than those achieved using pristine ISS, respectively. Photochemical, photoelectrochemical and photophysical measurements confirmed that the ISS/CBB photocatalyst exhibited effective electron transfer from ISS to CBB as well as excellent long-lifetime carrier separation properties owing to the built-up interfacial electric field. Moreover, based on in situ diffuse reflectance spectra and DFT calculations, ISS/CBB showed a decreased energy barrier for CO_2 reduction to CO via an adsorbed COOH^* intermediate, which facilitated the selective reduction of CO_2 to CO. The findings of this study shed light on the internal electric field engineering S-scheme-based heterojunction for improving CO_2 reduction and CO selectivity.

CRediT authorship contribution statement

Zhenzong Zhang: Conceptualization, Investigation, Formal analysis, Writing – review & editing, Software. **Meiyang Wang:** Investigation, Formal analysis. **Zexu Chi:** Investigation, Formal analysis. **Wenjie Li:** Investigation, Formal analysis. **Han Yu:** Conceptualization, Writing – review & editing. **Nan Yang:** Data Curation. **Hongbing Yu:** Conceptualization, Funding acquisition, Formal analysis, Writing – review & editing.

Declaration of Competing Interest

The authors declare no competing financial interests.

Acknowledgements

This work was supported by the National Basic Research Program of China (2016YFC0209301), Science and Technology Plans of Tianjin (17PTGCCX00250 and 15ZXGTSF00020) and Tianjin Development Program for Innovation and Entrepreneurship. The authors would like to thank Jian-ming Liu from Shiyanjia Lab (www.shiyanjia.com) for the language editing service.

Appendix A. Supporting information

Supplementary data associated with this article can be found in the online version at [doi:10.1016/j.apcatb.2022.121426](https://doi.org/10.1016/j.apcatb.2022.121426).

References

- [1] H. Ostovari, L. Müller, J. Skocek, A. Bardow, From unavoidable CO_2 source to CO_2 sink? a cement industry based on CO_2 mineralization, *Environ. Sci. Technol.* 55 (2021) 5212–5223, <https://doi.org/10.1021/acs.est.0c07599>.
- [2] W.J. van Hoek, J. Wang, L. Vilmin, A.H.W. Beusen, J.M. Mogollón, G. Müller, P. A. Pika, X. Liu, J.J. Langeveld, A.F. Bouwman, J.J. Middelburg, Exploring spatially explicit changes in carbon budgets of global river basins during the 20th Century, *Environ. Sci. Technol.* 55 (2021) 16757–16769, <https://doi.org/10.1021/acs.est.1c04605>.
- [3] I. Sullivan, A. Goryachev, I.A. Digdaya, X. Li, H.A. Atwater, D.A. Vermaas, C. Xiang, Coupling electrochemical CO_2 conversion with CO_2 capture, *Nat. Catal.* 4 (2021) 952–958, <https://doi.org/10.1038/s41929-021-00699-7>.
- [4] X. Chang, T. Wang, J. Gong, CO_2 photo-reduction: insights into CO_2 activation and reaction on surfaces of photocatalysts, *Energy Environ. Sci.* 9 (2016) 2177–2196, <https://doi.org/10.1039/C6EE00383D>.
- [5] S. Wang, A.A. Tountas, W. Pan, J. Zhao, L. He, W. Sun, D. Yang, G.A. Ozin, CO_2 footprint of thermal versus photothermal CO_2 catalysis, *Small* 17 (2021), 2007025, <https://doi.org/10.1002/sml.202007025>.
- [6] J. Wu, Y. Huang, W. Ye, Y. Li, CO_2 reduction: from the electrochemical to photochemical approach, *Adv. Sci.* 4 (2017), 1700194, <https://doi.org/10.1002/advs.201700194>.
- [7] H. Wang, Z. Liang, M. Tang, G. Chen, Y. Li, W. Chen, D. Lin, Z. Zhang, G. Zhou, J. Li, Z. Lu, K. Chan, T. Tan, Y. Cui, Self-selective catalyst synthesis for CO_2 Reduction, *Joule* 3 (2019) 1927–1936, <https://doi.org/10.1016/j.joule.2019.05.023>.
- [8] G.W. Woyessa, J.-a B. dela Cruz, M. Rameez, C.-H. Hung, Nanocomposite catalyst of graphitic carbon nitride and Cu/Fe mixed metal oxide for electrochemical CO_2 reduction to CO, *Appl. Catal. B: Environ.* 291 (2021), 120052, <https://doi.org/10.1016/j.apcatb.2021.120052>.
- [9] J. Wang, S. Lin, N. Tian, T. Ma, Y. Zhang, H. Huang, Nanostructured metal sulfides: classification, modification strategy, and solar-driven CO_2 reduction application, *Adv. Funct. Mater.* 31 (2020), 2008008, <https://doi.org/10.1002/adfm.202008008>.
- [10] X. Xiong, Y. Zhao, R. Shi, W. Yin, Y. Zhao, G.I.N. Waterhouse, T. Zhang, Selective photocatalytic CO_2 reduction over Zn-based layered double hydroxides containing tri- or tetravalent metals, *Sci. Bull.* 65 (2020) 987–994, <https://doi.org/10.1016/j.scib.2020.03.032>.
- [11] H. Jiang, K.-i Katsumata, J. Hong, A. Yamaguchi, K. Nakata, C. Terashima, N. Matsushita, M. Miyauchi, A. Fujishima, Photocatalytic reduction of CO_2 on Cu_2O -loaded Zn-Cr layered double hydroxides, *Appl. Catal. B: Environ.* 224 (2018) 783–790, <https://doi.org/10.1016/j.apcatb.2017.11.011>.
- [12] X. Li, S. Wang, L. Li, Y. Sun, Y. Xie, Progress and perspective for in situ studies of CO_2 reduction, *J. Am. Chem. Soc.* 142 (2020) 9567–9581, <https://doi.org/10.1021/jacs.0c02973>.
- [13] J. Ran, M. Jaroniec, S. Qiao, Cocatalysts in semiconductor-based photocatalytic CO_2 reduction: achievements, challenges, and opportunities, *Adv. Mater.* 30 (2018), 1704649, <https://doi.org/10.1002/adma.201704649>.
- [14] Y. Chai, Y. Chen, J. Shen, M. Ni, B. Wang, D. Li, Z. Zhang, X. Wang, Distortion of the coordination structure and high symmetry of the crystal structure in In_4SnS_8 microflowers for enhancing visible-light photocatalytic CO_2 reduction, *ACS Catal.* 11 (2021) 11029–11039, <https://doi.org/10.1021/acscatal.1c02937>.
- [15] S. Zhang, J. Hong, X. Zeng, J. Hao, Y. Zheng, Q. Fan, W.K. Pang, C. Zhang, T. Zhou, Z. Guo, Constructing layered nanostructures from non-layered sulfide crystals via surface charge manipulation strategy, *Adv. Funct. Mater.* 31 (2021), 202101676, <https://doi.org/10.1002/adfm.202101676>.
- [16] Y. Xia, J. Yu, Reaction: rational design of highly active photocatalysts for CO_2 conversion, *Chem* 6 (2020) 1039–1040, <https://doi.org/10.1016/j.chempr.2020.02.015>.
- [17] Q. Xu, L. Zhang, B. Cheng, J. Fan, J. Yu, S-scheme heterojunction photocatalyst, *Chem* 6 (2020) 1–17, <https://doi.org/10.1016/j.chempr.2020.06.010>.
- [18] S. Chatterjee, U. Maitra, In situ formation of luminescent CdSe QDs in a metalhydrogel: a strategy towards synthesis, isolation, storage and re-dispersion of the QDs, *Nanoscale* 9 (2017) 13820–13827, <https://doi.org/10.1039/C7NR03758A>.
- [19] S. Huang, C. Yeh, G. Chen, M. Liu, H. Chen, Investigation of luminescence enhancement and decay of QD-LEDs: interface reactions between QDs and

- atmospheres, *ACS Appl. Mater. Interfaces* 11 (2019) 2516–2525, <https://doi.org/10.1021/acsami.8b18558>.
- [20] Z. Dong, Z. Zhang, Y. Jiang, Y. Chu, J. Xu, Embedding CsPbBr₃ perovskite quantum dots into mesoporous TiO₂ beads as an S-scheme heterojunction for CO₂ photoreduction, *Chem. Eng. J.* 433 (2021), 133762, <https://doi.org/10.1016/j.cej.2021.133762>.
- [21] F. Maddalena, M.E. Witkowski, M. Makowski, A. Bachiri, B. Mahler, Y. Wong, C.Y. E. Chua, J.X. Lee, W. Drozdowski, S.V. Springham, C. Dujardin, M.D. Birowosuto, C. Dang, Stable and bright commercial CsPbBr₃ quantum dot-resin layers for apparent X-ray imaging screen, *ACS Appl. Mater. Interfaces* 13 (2021) 59450–59459, <https://doi.org/10.1021/acsami.1c16171>.
- [22] X. Xiong, C. Mao, Z. Yang, Q. Zhang, G.I.N. Waterhouse, L. Gu, T. Zhang, Photocatalytic CO₂ reduction to CO over Ni single atoms supported on defect-rich zirconia, *Adv. Energy Mater.* 10 (2020), 2002928, <https://doi.org/10.1002/aenm.202002928>.
- [23] J. Wang, L. Xu, T. Wang, R. Li, Y. Zhang, J. Zhang, T. Peng, Porphyrin conjugated polymer grafted onto bivo₄ nanosheets for efficient Z-scheme overall water splitting via cascade charge transfer and single-atom catalytic sites, *Adv. Energy Mater.* 11 (2021), 2003575, <https://doi.org/10.1002/aenm.202003575>.
- [24] Q. Li, T. Song, Y. Zhang, Q. Wang, Y. Yang, Boosting photocatalytic activity and stability of lead-free Cs₃Bi₂Br₉ perovskite nanocrystals via in situ growth on monolayer 2D Ti₃C₂T_x MXene for C–H bond oxidation, *ACS Appl. Mater. Interfaces* 13 (2021) 27323–27333, <https://doi.org/10.1021/acsami.1c06367>.
- [25] Z. Ji, Y. Liu, W. Li, C. Zhao, W. Mai, Reducing current fluctuation of Cs₃Bi₂Br₉ perovskite photodetectors for diffuse reflection imaging with wide dynamic range, *Sci. Bull.* 65 (2020) 1371–1379, <https://doi.org/10.1016/j.scib.2020.04.018>.
- [26] G. Zuo, Y. Wang, W.L. Teo, Q. Xian, Y. Zhao, Direct Z-scheme TiO₂–ZnIn₂S₄ nanoflowers for cocatalyst-free photocatalytic water splitting, *Appl. Catal. B: Environ* 291 (2021), 120126, <https://doi.org/10.1016/j.apcatb.2021.120126>.
- [27] Y. Lei, G. Wang, L. Zhou, W. Hu, S. Song, W. Fan, H. Zhang, Cubic spinel In₄SnS₈: electrical transport properties and electrochemical hydrogen storage properties, *Dalton Trans.* 39 (2010) 7021–7024, <https://doi.org/10.1039/C0DT00060D>.
- [28] P. Xia, S. Cao, B. Zhu, M. Liu, M. Shi, J. Yu, Y. Zhang, Designing 0D/2D S-scheme heterojunction over polymeric carbon nitride for visible-light photocatalytic inactivation of bacteria, *Angew. Chem. Int. Ed.* 59 (2020) 5218–5225, <https://doi.org/10.1002/anie.201916012>.
- [29] A. Meng, B. Cheng, H. Tan, J. Fan, C. Su, J. Yu, TiO₂/polydopamine S-scheme heterojunction photocatalyst with enhanced CO₂ reduction selectivity, *Appl. Catal. B: Environ* 289 (2021), 120039, <https://doi.org/10.1016/j.apcatb.2021.120039>.
- [30] J. Sheng, Y. He, J. Li, C. Yuan, H. Huang, S. Wang, Y. Sun, Z. Wang, F. Dong, Identification of halogen-associated active sites on bismuth-based perovskite quantum dots for efficient and selective CO₂-to-CO photoreduction, *ACS. Nano* 14 (2020) 13103–13114, <https://doi.org/10.1021/acsnano.0c04659>.
- [31] C. Liu, Y. Wang, H. Geng, T. Zhu, E. Ertekin, D. Gosztola, S. Yang, J. Huang, B. Yang, K. Han, S.E. Canton, Q. Kong, K. Zheng, X. Zhang, Asynchronous photoexcited electronic and structural relaxation in lead-free perovskites, *J. Am. Chem. Soc.* 141 (2019) 13074–13080, <https://doi.org/10.1021/jacs.9b04557>.
- [32] Z. Wang, Q. Wan, Y. Shi, H. Wang, Y. Kang, S. Zhu, S. Lin, L. Wu, Selective photocatalytic reduction CO₂ to CH₄ on Ultrathin TiO₂ nanosheet via coordination activation, *Appl. Catal. B: Environ* 288 (2021), 120000, <https://doi.org/10.1016/j.apcatb.2021.120000>.
- [33] Y. Liu, D. Shen, Q. Zhang, Y. Lin, F. Peng, Enhanced photocatalytic CO₂ reduction in H₂O vapor by atomically thin Bi₂WO₆ nanosheets with hydrophobic and nonpolar surface, *Appl. Catal. B: Environ* 283 (2021), 119630, <https://doi.org/10.1016/j.apcatb.2020.119630>.
- [34] S. Wang, B.Y. Guan, Y. Lu, X.W.D. Lou, Formation of hierarchical In₂S₃–CdIn₂S₄ heterostructured nanotubes for efficient and stable visible light CO₂ reduction, *J. Am. Chem. Soc.* 139 (2017) 17305–17308, <https://doi.org/10.1021/jacs.7b10733>.
- [35] H. Wu, X.Y. Kong, X. Wen, S.P. Chai, E.C. Lovell, J. Tang, Y.H. Ng, Metal-organic frameworks decorated cuprous oxide nanowires for long-lived charges applied in selective photocatalytic CO₂ reduction to CH₄, *Angew. Chem. Int. Ed.* 60 (2020) 8455–8459, <https://doi.org/10.1002/anie.202015735>.
- [36] K. Wang, L. Jiang, X. Wu, G. Zhang, Vacancy mediated Z-scheme charge transfer in a 2D/2D La₂Ti₂O₇/g-C₃N₄ nanojunction as a bifunctional photocatalyst for solar-to-energy conversion, *J. Mater. Chem. A* 8 (2020) 13241–13247, <https://doi.org/10.1039/d0ta01310b>.
- [37] G. Yang, D. Chen, H. Ding, J. Feng, J.Z. Zhang, Y. Zhu, S. Hamid, D.W. Bahnemann, Well-designed 3D ZnIn₂S₄ nanosheets/TiO₂ nanobelts as direct Z-scheme photocatalysts for CO₂ photoreduction into renewable hydrocarbon fuel with high efficiency, *Appl. Catal. B: Environ* 219 (2017) 611–618, <https://doi.org/10.1016/j.apcatb.2017.08.016>.
- [38] Z. Wang, Y. Luo, T. Hisatomi, J.J.M. Vequizo, S. Suzuki, S. Chen, M. Nakabayashi, L. Lin, Z. Pan, N. Kariya, A. Yamakata, N. Shibata, T. Takata, K. Teshima, K. Domen, Sequential cocatalyst decoration on BaTaO₂N towards highly-active Z-scheme water splitting, *Nat. Commun.* 12 (2021) 1005, <https://doi.org/10.1038/s41467-021-21284-3>.
- [39] Z. Zhang, Y. Cao, F. Zhang, W. Li, Y. Li, H. Yu, M. Wang, H. Yu, Tungsten oxide quantum dots deposited onto ultrathin CdIn₂S₄ nanosheets for efficient S-scheme photocatalytic CO₂ reduction via cascade charge transfer, *Chem. Eng. J.* 428 (2022), 131218, <https://doi.org/10.1016/j.cej.2021.131218>.
- [40] Z. Pan, L. Qian, J. Shen, J. Huang, Y. Guo, Z. Zhang, Construction and application of Z-scheme heterojunction In₂O₃/Bi₄O₇ with effective removal of antibiotic under visible light, *Chem. Eng. J.* 426 (2021), 130385, <https://doi.org/10.1016/j.cej.2021.130385>.
- [41] Z. Zhang, Z. Pan, Y. Guo, P.K. Wong, X. Zhou, R. Bai, In-situ growth of all-solid Z-scheme heterojunction photocatalyst of Bi₂O₃/g-C₃N₄ and high efficient degradation of antibiotic under visible light, *Appl. Catal. B: Environ* 261 (2020), 118212, <https://doi.org/10.1016/j.apcatb.2019.118212>.
- [42] J. Shen, L. Qian, J. Huang, Y. Guo, Z. Zhang, Enhanced degradation toward Levofloxacin under visible light with S-scheme heterojunction In₂O₃/Ag₂CO₃: internal electric field, DFT calculation and degradation mechanism, *Sep. Purif. Technol.* 275 (2021), 119239, <https://doi.org/10.1016/j.seppur.2021.119239>.
- [43] F. Li, X. Yue, D. Zhang, J. Fan, Q. Xiang, Targeted regulation of exciton dissociation in graphitic carbon nitride by vacancy modification for efficient photocatalytic CO₂ reduction, *Appl. Catal. B: Environ* 292 (2021), 120179, <https://doi.org/10.1016/j.apcatb.2021.120179>.
- [44] Z. Zhang, Y. Zhao, J. Shen, Z. Pan, Y. Guo, P.K. Wong, H. Yu, Synthesis of 1D Bi₁₂O₁₇Cl₂Br_{2-x} nanotube solid solutions with rich oxygen vacancies for highly efficient removal of organic pollutants under visible light, *Appl. Catal. B: Environ* 269 (2020), 118774, <https://doi.org/10.1016/j.apcatb.2020.118774>.
- [45] Y. Lu, Y. Lin, T. Xie, L. Chen, S. Yi, D. Wang, Effect of photogenerated charge transfer on the photocatalysis in high-performance hybrid Pt-Co:ZnO nanostructure photocatalyst, *ACS Appl. Mater. Interfaces* 5 (2013) 4017–4020, <https://doi.org/10.1021/am4007484>.
- [46] M. Sayed, F. Xu, P. Kuang, J. Low, S. Wang, L. Zhang, J. Yu, Sustained CO₂-photoreduction activity and high selectivity over Mn, C-codoped ZnO core-triple shell hollow spheres, *Nat. Commun.* 12 (2021) 4936, <https://doi.org/10.1038/s41467-021-25007-6>.
- [47] J. Jiang, Z. Mu, H. Xing, Q. Wu, X. Yue, Y. Lin, Insights into the synergetic effect for enhanced UV/visible-light activated photodegradation activity via Cu-ZnO photocatalyst, *Appl. Surf. Sci.* 478 (2019) 1037–1045, <https://doi.org/10.1016/j.apsusc.2019.02.019>.
- [48] L.J. Zhang, S. Li, B.K. Liu, D.J. Wang, T.F. Xie, Highly efficient CdS/WO₃ photocatalysts: Z-Scheme photocatalytic mechanism for their enhanced photocatalytic H₂ evolution under visible light, *ACS. Catal.* 4 (2014) 3724–3729, <https://doi.org/10.1021/cs500794j>.
- [49] X. Wang, X. Wang, J. Huang, S. Li, A. Meng, Z. Li, Interfacial chemical bond and internal electric field modulated Z-scheme Sv-ZnIn₂S₄/MoSe₂ photocatalyst for efficient hydrogen evolution, *Nat. Commun.* 12 (2021) 4112, <https://doi.org/10.1038/s41467-021-24511-z>.
- [50] X. Wang, Y. Wang, M. Gao, J. Shen, X. Pu, Z. Zhang, H. Lin, X. Wang, BiVO₄/Bi₄Ti₃O₁₂ heterojunction enabling efficient photocatalytic reduction of CO₂ with H₂O to CH₃OH and CO, *Appl. Catal. B: Environ* 270 (2020), 118876, <https://doi.org/10.1016/j.apcatb.2020.118876>.
- [51] Y. Li, Q. Wu, Y. Chen, R. Zhang, C. Li, K. Zhang, M. Li, Y. Lin, D. Wang, X. Zou, T. Xie, Interface engineering Z-scheme Ti-Fe₂O₃/In₂O₃ photoanode for highly efficient photoelectrochemical water splitting, *Appl. Catal. B: Environ* 290 (2021), 120058, <https://doi.org/10.1016/j.apcatb.2021.120058>.
- [52] W. Wang, Y. Tao, L. Du, Z. Wei, Z. Yan, W.K. Chan, Z. Lian, R. Zhu, D.L. Phillips, G. Li, Femtosecond time-resolved spectroscopic observation of long-lived charge separation in bimetallic sulfide/g-C₃N₄ for boosting photocatalytic H₂ evolution, *Appl. Catal. B: Environ* 282 (2021), 119568, <https://doi.org/10.1016/j.apcatb.2020.119568>.
- [53] F. Xu, K. Meng, B. Cheng, S. Wang, J. Xu, J. Yu, Unique S-scheme heterojunctions in self-assembled TiO₂/CsPbBr₃ hybrids for CO₂ photoreduction, *Nat. Commun.* 11 (2020) 4613, <https://doi.org/10.1038/s41467-020-18350-7>.
- [54] L. Li, C. Guo, J. Ning, Y. Zhong, D. Chen, Y. Hu, Oxygen-vacancy-assisted construction of FeOOH/CdS heterostructure as an efficient bifunctional photocatalyst for CO₂ conversion and water oxidation, *Appl. Catal. B: Environ* 293 (2021), 120203, <https://doi.org/10.1016/j.apcatb.2021.120203>.